Biosensors and Bioelectronics 222 (2023) 114979

Contents lists available at ScienceDirect

Biosensors and Bioelectronics

journal homepage: www.elsevier.com/locate/bios

High-intensity vector signals for detecting SARS-CoV-2 RNA using CRISPR/Cas13a couple with stabilized graphene field-effect transistor

Yang Sun [a], Cheng Yang [b], Xiaolin Jiang [d], Pengbo Zhang [a], Shuo Chen [b], Fengxia Su [a], Hui Wang [a], Weiliang Liu [a], Xiaofei He [a], Lei Chen [c,***], Baoyuan Man [b,**], Zhengping Li [a,*]

[a] Department of Chemistry and Biological Engineering, University of Science and Technology Beijing 30 Xueyuan Road, Haidian District, Beijing, 100083, PR China
[b] Department of Physics and Electronics, Shandong Normal University 1 Daxue Road, Changqing District, Jinan, Shandong Province, 250014, PR China
[c] Department of of Life Sciences, Shandong Normal University 1 Daxue Road, Changqing District, Jinan, Shandong Province, 250014, PR China
[d] Shandong Provincial Key Laboratory of Communicable Disease Control and Prevention, Shandong Center for Disease Control and Prevention, 16992 Jingshi Road, Lixia District, Jinan, Shandong Province, 250014, PR China

ARTICLE INFO

Keywords:
Vector signal
SARS-CoV-2 detection
Stabilized graphene field-effect transistor
CRISPR/Cas13a
Amplification-free

ABSTRACT

False detection of SARS-CoV-2 is detrimental to epidemic prevention and control. The scalar nature of the detected signal and the imperfect target recognition property of developed methods are the root causes of generating false signals. Here, we reported a collaborative system of CRISPR-Cas13a coupling with the stabilized graphene field-effect transistor, providing high-intensity vector signals for detecting SARS-CoV-2. In this collaborative system, SARS-CoV-2 RNA generates a "big subtraction" signal with a right-shifted feature, whereas any untargets cause the left-shifted characteristic signal. Thus, the false detection of SARS-CoV-2 is eliminated. High sensitivity with 0.15 copies/μL was obtained. In addition, the wide concerned instability of the graphene field-effect transistor for biosensing in solution environment was solved by the hydrophobic treatment to its substrate, which should be a milestone in advancing it's engineering application. This collaborative system characterized by the high-intensity vector signal and amazing stability significantly advances the accurate SARS-CoV-2 detection from the aspect of signal nature.

1. Introduction

The characteristics of human-to-human transmission and a high proportion of asymptomatic infections caused the severe acute respiratory syndrome coronavirus 2 (SARS-CoV-2) spread rapidly and large-scale outbreaks worldwide, posing a massive threat to public health (Arons et al., 2020; Boyton and Altmann, 2021). The severe epidemic has prompted scientists to explore various strategies for SARS-CoV-2 detection (Kevadiya et al., 2021; Orooji et al., 2021), such as surface-enhanced Raman spectroscopy (Yang et al., 2021; Sitjar et al., 2021), microfluidic integrated biochip (Swank et al., 2021; Welch et al., 2022), colorimetric assay (Talebian et al., 2020), loop-mediated isothermal amplification (Bokelmann et al., 2021), and real-time reverse transcription-polymerase chain reaction (RT-PCR) (Liu et al., 2020; Smyrlaki et al., 2020). These works have actively promoted the detection of SARS-CoV-2 from different aspects.

Determining the intensity of the detected signal is the primary basis for these reported strategies to distinguish positive samples from negative samples. However, the low abundance of biomarkers in mildly or asymptomatic positive patients and the unperfect detection mechanism focusing on signal intensity alone, leading to the detected signal may be false-negative or false-positive (Cohen et al., 2020; Long et al., 2020; Nath et al., 2021; Song et al., 2020; Woloshin et al., 2020). Inaccurate test results have brought a lot of inconvenience to people's health, finance, education, and psychological convenience, affecting the government's decision-making and causing unnecessary loss of social resources (Surkova et al., 2020). The root cause of false-negative signals is that trace biomarkers cannot effectively generate high-intensity detectable signals. The root cause of false-positive signals is that the reported detection signals are scalar signals rather than vector signals, where untargeted biomarkers can generate similar-intensity signals to target biomarkers. Suppose the signal generation ability of trace target

* Corresponding author.
** Corresponding author.
*** Corresponding author.
E-mail addresses: chenlei@sdnu.edu.cn (L. Chen), byman@sdnu.edu.cn (B. Man), lzpbd@ustb.edu.cn (Z. Li).

https://doi.org/10.1016/j.bios.2022.114979
Received 7 October 2022; Received in revised form 25 November 2022; Accepted 29 November 2022
Available online 30 November 2022
0956-5663/© 2022 Elsevier B.V. All rights reserved.

biomarkers can be amplified and the detected signals could have a directional characteristic in addition to the intensity characteristics alone, it will undoubtedly strongly prevent the false detection results.

Hailed by nature as one of the seven technologies that will majorly impact science in 2022 (Eisenstein, 2022), the clustering regularly interspaced short palindromic repeats (CRISPR) based diagnostic technology, especially the CRISPR-Cas13a system, has shown significant advantages in the field of virus diagnosis and attracted widespread attention (Kaminski et al., 2021; Tang et al., 2021). SARS-CoV-2 is a positive-strand RNA virus (Chan et al., 2020). For the CRISPR-Cas13a system, the CRISPR is a programmable spacer sequence that can recognize target RNA with single-base mismatch specificity and activates the Cas13a. The activated Cas13a performs a "collateral cleavage" effect and could indiscriminately cleave any surrounding single-strand RNA molecules (Gootenberg et al., 2017). The impressive cleavage to RNA, high base resolution, and programmability upon nucleic acid recognition make the CRISPR-Cas13a system highly promising to specifically amplify the detection signal of SARS-CoV-2 RNA. Biosensors based on graphene field effect transistors (GFET) have attracted widespread attention in the rapid and high-precision detection of various diseases by analyzing nucleic acid information due to their abundant analyzable signals, short response time, high sensitivity, and low cost. In recent years, the rapid and sensitive detection of SARS-CoV-2 (Wang et al., 2022a), Alzheimer's disease, Down's trisomy, and various cancers has been effectively realized by GFET biosensors (Bonanni et al., 2012; Liu et al., 2019; Mao et al., 2017). For the GFET, graphene shows a strong ambipolar electric field effect (Novoselov et al., 2004), where the exogenous electron doping makes graphene's Dirac point move to the left and the exogenous hole doping makes graphene's Dirac point move to the right (Chen et al., 2009). Type change of exogenous doping modulates the Dirac point to move in different directions (Ang et al., 2008). In addition, graphene's high carrier mobility and good electrical conductivity make the Dirac point change significantly responding to minor charge disturbances on the graphene's surface (Schedin et al., 2007). These make GFET could sensitively detect charged molecules (such as RNA or DNA) through a directional signal.

Here, we reported a collaborative system of CRISPR-Cas13a coupling with graphene field-effect transistor for detecting SARS-CoV-2 RNA by generating a high-intensity vectorized signal. CRISPR-Cas13a system makes the detected signal with high intensity, and the GFET makes the detected signal directional. In this collaborative system, the reporter probes (RP) are saturable bound to the graphene surface and dope the graphene with the electron, making Dirac point shift to the left. CRISPR-Cas13a activated by SARS-CoV-2 RNA can massively cleavage the reporter probes and sharply attenuate the reporter probe's electron doping to graphene, resulting in an amplified signal with a significant right shift of the Dirac point and thus generating a "big subtraction" signal. Inability to activate CRISPR-Cas13a and unspecific adsorption with graphene, make untargeted molecules play the same role as reporter probes, doping graphene with electrons and making the Dirac point furtherly shift to the left. Thus, the false results for detecting SARS-CoV-2 can be effectively eliminated by the opposite signal direction. As a result, high sensitivity as low as 0.15 copies/ μL was obtained. More importantly, as well known, the instability of graphene field-effect transistor resulting from the time-dependent left shift of graphene Dirac point in analytical liquid is one of the most important factors that plague it's practicability for many years. In this work, we firstly found that hydrophobic treatment of the field-effect transistor's substrate can successfully eliminate this instability, which should be a milestone in advancing the reliable application of the field-effect transistor in biosensing.

2. Material and methods

2.1. Reagents

LawCas13a protein was purchased from HuicH (Shanghai, China). 10XNEB buffer r2.1 was purchased from NEW ENGLAND BioLabs Inc. (Ipswich, UK). Recombinant RNase Inhibitor (RRI), DEPC-treated water, DNase I, Taq DNA Polymerase, dNTP mixture, NTP mixture, forward primer and reverse primer were obtained from TaKaRa Biotechnology Co., Ltd. (Dalian, China). T7 RNA Polymerase was purchased from New England Biolabs (Beijing, China). RNA clean Kit was obtained from TIANGEN Biotech (Beijing) Co., Ltd. EZ-10 Spin Column Viral Total RNA Extraction Kit acquired from Sangon Biotech (Shanghai, China). The indium tin oxide (ITO)/SiO_2 substrate was purchased from GULUO GLASS (Luo yang) Co., Ltd. 1-Pyrenebutanoic acid succinimidyl ester (PBASE), ethanolamine, n-octadecyl trichlorosilane (OTS), and Dimethylsulfoxide (DMSO) were purchased from Aladdin Co., Ltd. The detailed information on the used nucleic acids in this work is shown in Table S1.

2.2. Immobilization of RP

PBASE functionalized the fabricated GFET to immobilize the RP. The pyrene group of PBASE can bind with graphene by π-π stacking and thus form a self-assembled uniformly monolayer film on graphene surface (Hinnemo et al., 2017; Zhang et al., 2007), as show in Fig. S1. Then the 5′ terminus amine group-modified RP consisting of 5 uracil ribonucleotides (U) at 5′ terminus and 16 thymine deoxyribotides at 3′ terminus, were immobilized on the GFET surface through the conjugation reaction between the amine group and the amine-reactive succinimide group of PBASE (Fig. S2). The functionalization and immobilization results were characterized by transfer characteristic curve, X-ray photoelectron spectroscopy (XPS), and Raman spectrum. Firstly, after PBASE functionalization, the Dirac point, value of V_{GS} corresponding to minimum I_{DS}, exhibits an obvious right shift from 73 mV to 121 mV (Fig. S3, orange line), which is due to its pyrene group causing hole doping to graphene. Negatively charged RP contribute electron doping to graphene, making the Dirac point left-shifted from 121 mV to 76 mV when finishing the immobilization process (Fig. S3, purple line). In addition, the gradual decrease in the sharpness of the resistivity near the Dirac point also indicates the successful functionalization and immobilization (Tan et al., 2007). Secondly, the Raman spectrum, which is sensitive to doping (Das et al., 2008), was selected to characterize the functionalization and immobilization processes further. The fingerprint 2D peak of graphene shifts by 13 cm^{-1} to a positive direction after PBASE modification (Figs. S4A–4B), indicating graphene was effectively functionalized and has been hole-doped (Das et al., 2008; Wu et al., 2017). Then, the position of the 2D peak shifts by 5 cm^{-1} to a negative direction after reacting with the RP (Figs. S4B–4C), indicating RP was successfully immobilized and graphene has been electron-doped (Das et al., 2008; Wu et al., 2017). XPS of the functionalized graphene shows the clear N 1s peak, C-N, and C═N, which is caused by the N element in the Pyrene group of PBASE (Fig. S5A). The significant P 2p peak appears upon RP immobilization since RP consists of the P element (Fig. S5B). The above characterizations reveal the successful functionalization of graphene and the immobilization of RP. Here,the process of PBASE functionalizing graphene was finished in two steps instead of one step in the conventional method. Detailly, the pure graphene channel first reacts with PBASE solution in 30 min and then reacts with new PBASE solution in another 30 min after DMSO flushing. The two-step method shows a larger change of Dirac point than the one-step method with the same reaction time (Figs. S6A–6B). Similarly, the RP was also immobilized on the graphene surface by a two-step method. In the first step, 50 μL of the RP solution at a concentration of 10 mM was added to the liquid storage tank to react with PBASE. After 3 h, the liquid storage tank was rinsed several times with RNase-free water. In the second step, another 50 μL of

the RP solution with a concentration of 10 mM was added again to the liquid storage tank to react with graphene for 3 h at room temperature.

2.3. Fabrication of proposed GFET

Details about preparing graphene was described in text S1 and Fig. S7. The fabrication process of liquid-gated large-scale graphene field-effect transistor based on hydrophobic substrate consists of 10 steps (Fig. S8). The scale of obtained graphene/copper foil is 5 cm × 10 cm. Step 1: the integral graphene/copper was cut as several small graphene/Copper samples with a scale of 0.8 cm × 1.2 cm (Fig. S8A). Step 2: The acetone solution of polymethyl methacrylate (PMMA) was spin-coated on the surface of the graphene/copper sample. After drying at $100^{o}C$ for 1 h, PMMA film was formed to serve as the support layer for transferring graphene (Fig. S8B). Step 3: Put the PMMA/graphene/copper foil sample on the surface of the ferric chloride solution to etch the copper foil away (Fig. S8C). Step 4: After completing the etching step, the PMMA/graphene samples are transferred to the surface of deionized water by the coverslip for cleaning $FeCl_3$ and $CuCl_2$, and the cleaning process was repeated three times (Fig. S8D). To make the graphene field-effect transistor stable in solution, the substrate of the graphene field-effect transistor (glass substrate coated with ITO on both sides of the surface) was modified with hydrophobic function. Step 5: The substrates and 10 mL tubes were pre-dried at 70 °C for 1 h (Fig. S8E). Step 6: The substrate and 1% OTS solution were loaded into the pre-dried 10 mL tube and reacted for 20 min (Fig. S8F). Note that the 10 mL tube should be protected from light. After the modification process, the hydrophobic substrate was rinsed with toluene, acetone, alcohol, and deionized water. Step 7: The PMMA/graphene samples floating on the surface of deionized water were fished up with the hydrophobic substrate. During the fishing process, the PMMA/graphene sample should be accurately connected to the ITO electrodes on both sides of the glass substrate surface (Fig. S8G). Step 8: The PMMA/graphene/substrate sample was heated at 130 °C for 1.5 h to bond the graphene to the substrate surface (Fig. S8H). Step 9: To fully remove PMMA, the PMMA/graphene/substrate samples were soaked in acetone overnight (Fig. S8I). The graphene/substrate samples were washed sequentially with acetone, alcohol, and deionized water to obtain pure graphene. Step 10: The homemade polymethyl methacrylate liquid storage tank was pasted precisely above the graphene with UV-curable glue. Up to here, the liquid-gate large-scale graphene field-effect transistor based on the hydrophobic substrate is completed (Fig. S8J).

2.4. The collaborative system for detecting SARS-COV-2 RNA

Before using this collaborative system to detect SARS-CoV-2 RNA, it is necessary to mix SARS-CoV-2 RNA and CRISPR-Cas13a system in advance and pre-react in a test tube at 37 °C for 1 h to ensure that the RNP is fully activated. In addition, the pre-reaction could make the large-size targets were fully degraded before adding to GFET, avoiding the Cas13 enzymes be trapped on the sensor surface by the unspecific interaction between the large-size targets and the graphene. As shown in Fig. S9, the activated CRISPR-Cas13a system after 1 h pre-reaction just work to cleavage the reporter probes and would not contribute any unspecific absorption. After 1 h the pre-reaction, the mixed solution was mixed again and added to the liquid storage tank of GFET to react with the RP at 37 °C for 2 h, where the liquid storage tank should be sealed to avoid interference from the external environment. The detailed component of the mixture is shown in Table S2.

3. Results and discussion

The shift of Dirac points (Δ_{DP}) has been widely chosen as the characteristic signal for graphene field-effect transistor sensors to detect biomarkers (Gao et al., 2018; Hwang et al., 2020; Wang et al. 2019, 2021, 2022b). However, the Dirac point will spontaneously shift over time in solution (Gao et al., 2022; Hu et al., 2019), which causes extreme noise to the detected signal. The Dirac point of traditional GFET undergoes a clear left shift in 4 h without adding any target biomarkers to the test solution, and the maximum difference is 63 mV (Fig. 1A). Water in the test solution can penetrate the graphene and form a sub-nanometer-thin icelike film between the graphene and the substrate (Hong et al., 2019; Lee et al. 2012, 2014). Icelike water film modulates the charge transfer between graphene and the substrate, and it's thickness would increase with a positive charge and decrease with a negative charge (Chiu et al., 2019; Dollekamp et al., 2017; Hong et al., 2019). For GFET, the sweep gate voltage (charge varies from −1 v to 1 v) is a necessary condition for reading the Dirac point. Thus, the presence of the icelike water film makes it impossible to accurately determine that the detected signal is entirely caused by the target biomarkers, resulting in unconvincing detection results. We found that the hydrophobic treatment to GFET substrate can effectively solve this instability. Here, the substrate of GFET was treated by OTS, whose alkyl chain could form a hydrophobic film on the substrate, preventing the formation of the icelike water film between graphene and substrate (Fig. S10). The hydrophobic modification can be simply and quickly completed by immersing the graphene substrate in the toluene solution of OTS for 20 min. The liquid contact angle of the graphene substrate changed from 26 $^{\circ}C$ to 105 $^{\circ}C$ after hydrophobic modification (Fig. S11). Benefiting from the hydrophobic treatment, the Dirac point almost keeps a constant with a low RSD (1.1%) even if the GFET was immersed in a liquid environment for 31 h (Fig. 1B). Improving the stability of graphene in solution environment is a necessary technological breakthrough to promote reliable biosensing for GFET.

The working principle of this collaborative system for detecting SARS-COV-2 RNA is illustrated in Fig. 2. CRISPR contains a single stem-loop domain (Tracr RNA) that could specifically bind to Cas13a protein and a protospacer domain (Guide RNA, gRNA) which can specifically recognize the target sites of SARS.

-COV-2 RNA (Fig. 2A). In the absence of the target RNAs, CRISPR combines with Cas13a to form the nuclease-inactive ribonucleo protein (RNP). When the gRNA recognizes the target sites of SARS-COV-2 RNA, the nonspecific RNA cleavage activity of CRISPR-Cas13a is activated (Fig. 2B and C). Single activated RNP can indiscriminately degrade tens of thousands of RP. The GFET was employed as the sensor to detect the SARS-COV-2 RNA since graphene's ambipolar electric field effect could make the detected signal directional. The characterizations of GFET are detailed described in text S2 and Figs. S12–S13. The GFET was functionalized by PBASE to immobilize the RP(Fig. 2D–E). Electron doping to P-type graphene by the immobilized RP leads to an upward shift of the graphene Fermi level, resulting in an E signal (Figs. 2G, 1–2). In the presence of SARS-COV-2 RNA, the immobilized RP was massively cleaved by the activated RNP and left the graphene surface (Fig. 2F). RP's electron doping to graphene is sharply attenuated and the graphene Fermi level shifts downward, resulting in a "Cut-E″ signal (Fig. 2G, 2–3). Since untargeted molecules do not have the targeted site for the predesigned CRISPR, there is no activated RNP to cleavage the RP to generate a "Cut-E″ signal. Instead, untargeted molecules can unspecifically adsorb on graphene surface and act like the RP to electronically dope the graphene, resulting in an enlarged E signal. Experimentally, the E signal, enlarged E signal and "Cut-E″ signal can be determined by reading the Dirac point from the transfer characteristic curve of the GFET (text S3 and Fig. S14). The left shift of the Dirac point corresponds to the E signal or the enlarged E signal, and the right shift of the Dirac point corresponds to the "Cut-E″ signal. In conclusion, the directional "Cut-E″ signal generated by cutting the RP-induced E signal via SARS-COV-2 RNA-activated RNP is the indicator of whether the collaborative system has specifically and successfully detected the SARS-COV-2 RNA. It is worth mentioning that, unlike the RT-PCR method where the RP is uniformly dispersed in a solution with large size, the RP in this collaborative system is immobilized on the graphene surface with limited location, which facilitates its can be cleavaged more intensively

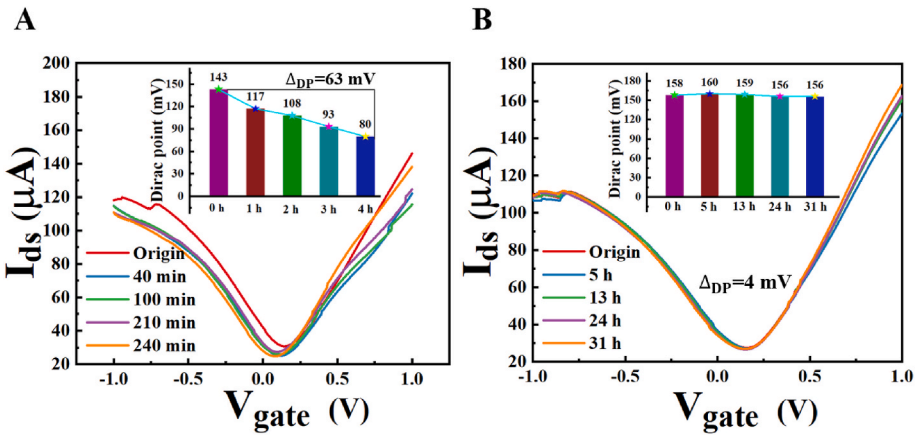


Fig. 1. Stability performance. The Dirac point shift over time of (A) traditional FET and (B) developed GFET with the hydrophobic-treated substrate.

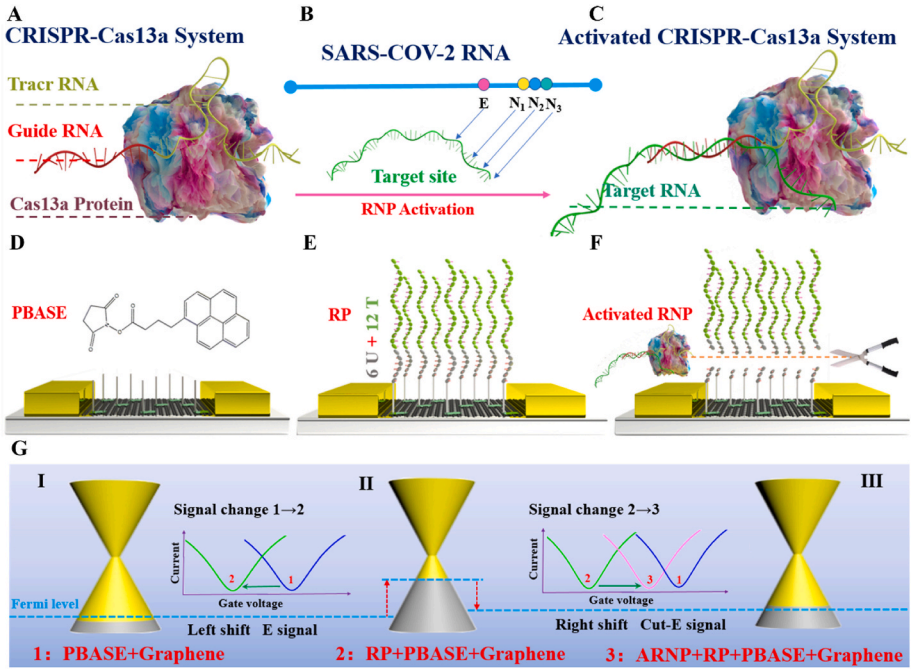


Fig. 2. Working principle of the collaborative system in detecting SARS-CoV-2 RNA. (A) Structure of CRISPR-Cas13a system including Trac RNA, Guide RNA, and Cas13a protein. (B-C) Mechanism that Cas13a protein is activated by Guide RNA recognizing the target sites of SARS-CoV-2 RNA. (D) Functionalization of graphene. (E) Immobilization of RP. (F) RP is cut away from graphene by activated RNP. (G) Mechanism of activated RNP (ARNP)-cleavage-mediated signal change. **I, II** and **III** are respectively the distribution of Fermi level from the immobilization to the cleavage of RP; Two inserts from left to right are the characteristic signal changes corresponding to Fermi level changes.

by the activated RNP. More importantly, the RP consisted of 6 ribonucleotides close to graphene and 16 deoxyribonucleotides away from graphene (Fig. 2E). If one ribonucleotide in the RP is cleavaged, at least 16 deoxyribonucleotides can be removed from the graphene surface (Fig. 2F). This dramatically increases signal generation efficiency compared to the RP composed entirely by ribonucleotides. The signal detection mechanism caused by the specific super cleavage properties of activated RNP to RP and the optimized RP structure bring a directional "big subtraction" signal for detecting SARS-COV-2 RNA.

The in vitro transcriptions N gene RNA of SARS-CoV-2 was first employed to evaluate this collaborative system's detection performance (text S4). Activating more RNP by one SARS-CoV-2 N gene RNA facilities the higher efficiency to cleavage RP and thus improves sensitivity (Fozouni et al., 2021). Here, three designed CRISPRs whose gRNA targets different sites of the same N gene RNA were used to complex with Cas13a protein to form three different RNP populations, making a single N gene RNA active 3 RNP (Fig. 3A). In the other hand, large E signal is facilized to detect and distinguish the "Cut-E″ signal caused by SARS-COV-2 RNA. Here, the RP was immobilized on the graphene surface by a two-step method rather than the conventional one-step method as described in method section, generating a larger E signal (Fig. 3B). The RP pre-reaction in the first step can extrude water molecules out of the graphene surface, which greatly reduces the repulsion of the water molecules on the graphene surface to the RP, thus improving the diffusion speed and the reaction efficiency of the RP in the second step (Elder and Jayaraman, 2013). To measure the sensitivity of this collaborative system, the immobilized RP were respectively cleavaged by the RNP activated by N gene RNA with concentrations changing from 0.1 aM to 100 aM. Each experiment was repeated ten times. After the RP & GFET reacted with the RNP activated by 0.1 aM N gene RNA (about 3 copies in 50 μL solution) for 2 h, the response signal (Cut-E/E %) was hardly generated (Fig. 3C and Fig. S15). The reason may be that such a low density of the activated RNPs make it difficult to fully diffuse to the graphene surface to generate an obviously "Cut-E″ signal within 2 h. Moreover, it is difficult to accurately pick up the N gene RNA molecules with 3 copies by dividing a certain volume of the solution. After the RP & GFET reacted with the RNP activated by 0.25 aM N gene RNA for 2 h, an unmistakable "Cut-E″ signal with 18 mV was generated (Fig. S16A), and the average cleavage efficiency of activated RNP to RP is 39.7% (Figs. 3C and 0.25 aM). The monitored results show a significant difference

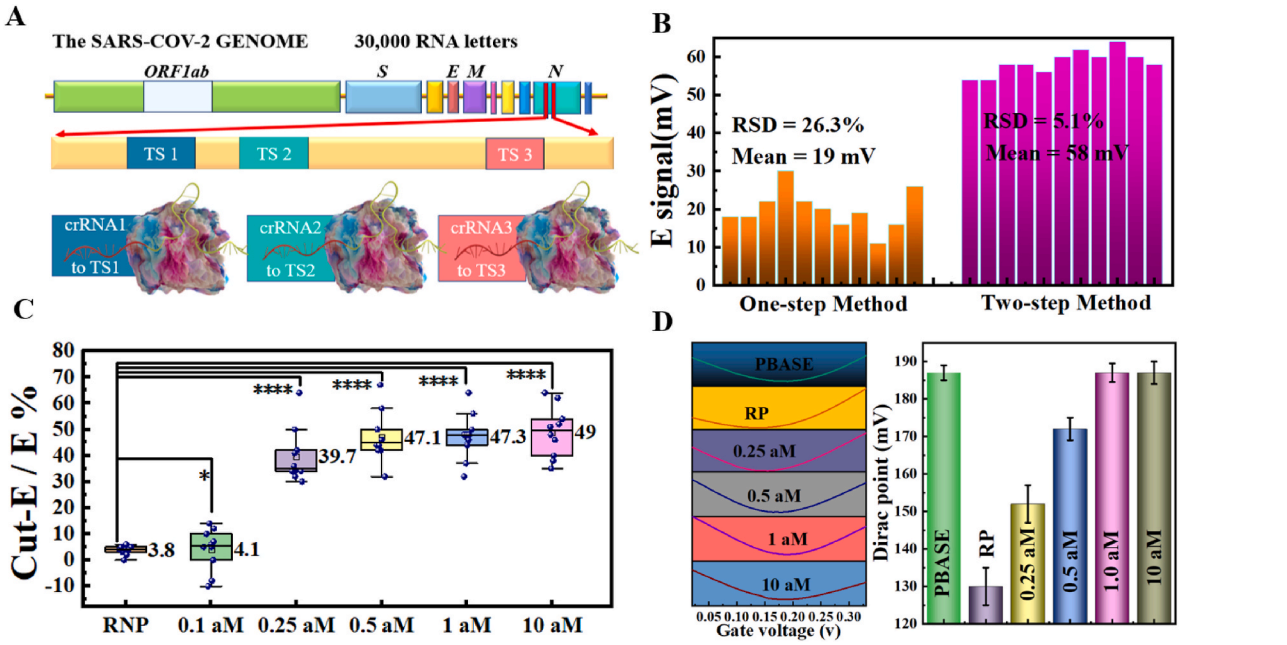


Fig. 3. SARS-CoV-2 N gene RNA testing. (A) Genome map of SARS-CoV-2 RNA and the target sites (TS) of N gene RNA to hybridize with gRNA. (B) Comparison of E signal induced by RP respectively in a one-step method and a two-step method to immobilize the RP. (C) Response of this collaborative system to detect SARS-CoV-2 N gene RNA with gradient concentration; Response signal (Cut-E/E %) were compared to the RNP control through an analysis of covariance (ANOVA): *$p > 0.5$, ****$p < 0.000001$, $P < 0.05$ indicates that there is a significant difference between N gene RNA and RNP. (D) Verifying the space-occupying effect: activated RNP sequentially cleavages the RP on the same device.

between 0.25 aM N gene and RNP with ****$p < 0.000001$, proving the detection limit of this collaborative system for detecting N gene RNA can easily reach 0.15 copies/ μL. 0.5 aM N gene RNA activats more RNP and thus cleavage more RP, resulting in a larger "Cut-E″ signal 27 mV (Fig. S16B), and the average cleavage efficiency of the activated RNP to RP is 47.1% (Figs. 3C and 0.5 aM). Logically, more E signals will be cut by growingly activated RNP and larger "Cut-E″ signals should generate, as N gene RNA concentration increases. However, when the RP & GFET reacted with the RNP activated by 1 aM N gene RNA and 10 aM N gene RNA for 2 h, the "Cut-E″ signal presented by 23 mV and 26 mV, respectively (Figs. S17A–17B), and the average cleavage efficiencies of activated RNP to RP were 47.3% and 49% (Figs. 3C and 1 aM-10 aM). There is almost no significant increase in the "Cut-E″ signal compared to the signal caused by the RNP activated by 0.5 aM N gene RNA. This can be explained by that the space-occupying effect make the density of activated RNP reach an upper limit on the surface of RP with the increasing activated RNP. The upper density makes the additional activated RNP be blocked in the outer layer and cannot directly interact with the RP.

The same device's E signal was orderly cut by the RNPs respectively activated by the N gene RNA with the concentration changing from 0.25 aM to 10 aM to verify the space-occupancy effect. Between every two cutting processes, there is a washing step. RNPs activated by a previous concentration of N gene RNA are washed off the RP surface while making room for RNPs activated by the next concentration of N gene RNA, thereby further cleavage the RP. In the experiment, an E signal of about 53 mV is formed by the immobilization of RP (Fig. 3D; PBASE-RP). After the RP & GFET reacted with the RNP activated by 0.25 aM N gene RNA for 2 h, an unmistakable "Cut-E″ signal with 16 mV occurred, and a 32% E signal was cut off (Fig. 3D; 0.25 aM). Following the wash step, the RNP activated by 0.5 aM N gene RNA was used to furtherly cut the E signal of the same device. The results showed that a 71% E signal was cut off (Fig. 3D; 0.5 aM). By the same steps, the E signal is 100% cut off after the RP & GFET reacted with RNP activated by 1 aM N gene RNA (Fig. 3D; 1 aM). The space-occupancy effect was effectively proved. By the way, there is no further change of Dirac point after the RP & GFET reacted with the RNP activated by 10 aM N gene RNA (Fig. 3D; 10 aM), demonstrating the activated RNP system does not contribute any unspecific effect to graphene, just work to cleavage RP.

Given its outstanding performance in detecting N gene RNA, the collaborative system was further applied to detect SARS-CoV-2 full-length RNA (Fig. 4A). Unlike N gene RNA, full-length RNA contains approximately 30,000 nucleotides (Chan et al., 2020; Liu et al., 2020). To fully exploit the signal-generating ability of these 30,000 nucleotides, another CRISPR whose gRNA targets the E gene RNA was added. The RNAs extracted from 6 RT-PCR confirmed positive samples were employed to characterize this collaborative system's sensitivity and reliability (Fig. S18 and text S5). The results show that this collaborative system exhibits the negative response signal in detecting 0.1 aM full-length RNA, which means enlarged E signals occurred and no generation of "Cut-E″ signals (Fig. 4B; 0.1 aM). We speculate that the enlarged E signal is caused by the strong unspecific adsorption between graphene and full-length RNA. Without sufficient activated RNP to fully cleavage these full-length RNAs, it can play the same role as the RP to contribute electron doping to graphene. Recently, some literature has verified this strong unspecific adsorption by studying the behaviour of oligonucleotides at the graphene−water interface using theoretical simulation (Cortés-Arriagada, 2021; Manna and Pati, 2013; Ranganathan et al., 2016). Here, we experimentally explored this unspecific adsorption. In the experiment, the full-length RNA was directly added to the graphene surface where there was no immobilization of specific probes. After reacting for 2 h, the graphene surface was flushed three times with RNase water. The results show that GFET generated a significant E signal about 25 mV (Fig. 4C), which proves full-length RNA can firmly bond to the graphene surface by unspecific interaction. This unspecific adsorption makes the traditional FET based on the hybridization-driven "small addition" signal generation mechanism face the challenge of signal purity in detecting long-chain nucleic acids, which simultaneously proves the superiority of the directional "big subtraction" signal generation mechanism of this collaborative system. This collaborative system exhibited approximately 42% E signal was cut off by the RNP activated by 0.25 aM full-length RNA (Fig. 4B; 0.25 aM).

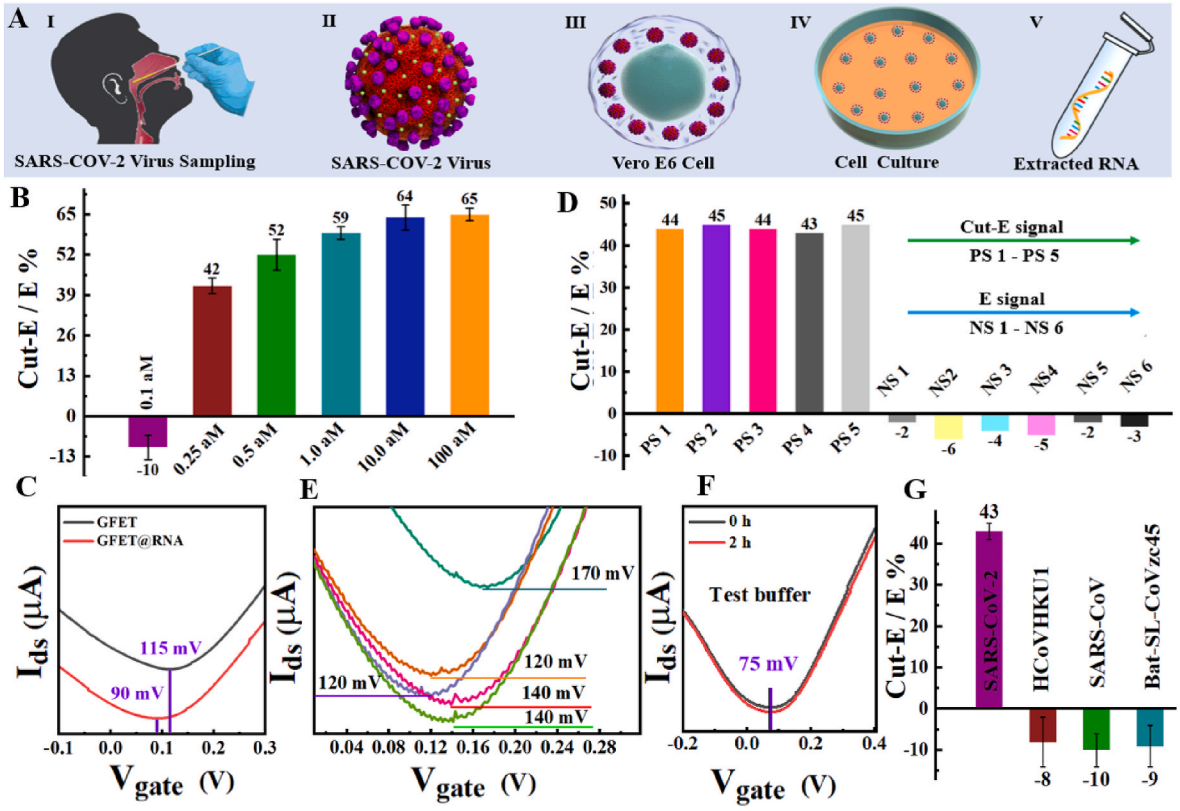


Fig. 4. Detection of SARS-CoV-2 full-length RNA. (A)Workflow of obtaining SARS-CoV-2 RNA from positive samples. (B) Response signal of this collaborative system to detect SARS-COV-2 RNA with increasing concentrations from 0.1 aM to 100 aM. (C) Untargeted molecules can absorb on graphene, causing enlarged E signal. (D) Response signals to SARS-CoV-2 RNA extracted from positive samples PS1−PS5 and negative samples NS1−NS6. (E-F) Specificity verification: RP cannot be degraded by test buffer or RNP mixture. (G) Specificity verification: Response signals to the RNAs of SARS-like coronavirus.

In the range of 0.25 aM–10 aM, the response signal grows with the increasing full-length RNA concentration (Fig. 4B; 0.25 aM–10 aM). Like N gene RNA assay results, the growing response signal stopped when RNP was activated by a higher concentration of 100 aM due to the space-occupying effect (Fig. 4B; 100 aM). 0.25 aM full-length RNAs extracted from the other five positive samples were independently tested. The results showed that these response signal's intensities were all about 44%, proving that this collaborative system has high sensitivity and excellent reproducibility for SARS-CoV-2 RNA detection (Fig. 4D; PS1-PS5). Notably, at any concentration, full-length RNA-activated RNP produced a more significant response signal than N gene-activated RNP in this collaborative system, which is caused by the additive effect of the CRISPR that targets E gene RNA. The RNAs extracted from six negative samples were also tested. Because these RNAs do not have the targeting site of the pre-designed CRISPR in this collaborative system, the RNP had not been activated and thus there is no generation of the "Cut-E″ signal instead of generating enlarged E signals by the unspecific adsorption (Fig. 4C; NS1-NS6). Thus the false-positive signal is eliminated by the opposite signal direction between the "Cut-E″ signal of targets and the enlarged E signals of untargets. The possibilities that RP has flushed away in the wash step or that the reading solution degraded RP were studied to prove that the "Cut-E″ signal is specifically generated by the full-length RNA. Since the collaborative system works in a 1 × NEB buffer where the salt concentration is 170 mM, the Debye length of the sensing graphene surface is only 0.74 nm, much shorter than the length of the RP (1.2 nm) (Stern et al., 2007). If we read the signal in the 1 × NEB buffer directly, some RP will exceed the Debye length and thus part RP cannot be effectively detected. Therefore, the 1× NEB buffer was flushed away and replaced by a 0.1× PBS buffer (reading solution) with a Debye length of 2.5 nm in the reading signal step. This would lead us to suspect that the RP was flushed away during the washing step instead of being cleavaged by the activated RNP during the step of reading the "Cut-E″ signal. To prove that, firstly, GFET & RP was flushed three times by reading solution. The result shows the Dirac points of GFET before and after flushing are the same, and there is almost no generation of the "Cut-E″ signal (Fig. 4E; RP-flushing), which proves that RP can be firmly bound to the graphene surface by PBASE and cannot be washed off. Secondly, the RNP activated by 0.5 aM full-length RNA was added and reacted with GFET & RP for 2 h. A significant "Cut-E″ signal with 21 mV was generated, and about 46% E signal was cut off (Fig. 4E; flushing-RNP). Finally, GFET & RP was rewashed three times by reading solution, the position of Dirac points had not changed, and there was no generation of the "Cut-E″ signal (Fig. 4E; RNP-flushing). The above progressive experiments demonstrated that the RP could not be affected by flushing steps. The Dirac point of GFET & RP were compared before and after reacting with the reading solution for 2 h h. The absence of a significant Dirac point shift suggests the RP cannot be degraded by the reading solution (Fig. 4F). The collaborative system also detected the RNAs extracted from three other SARS-like coronaviruses. Like negative sample assay results, the response signal is negative, suggesting the enlarged E signals were generated without generating any "Cut-E″ signal (Fig. 4G). In addition, the GFET sensor can still perform good ambipolar electric field effect and shows the similar response to the targets as the fresh GFET after 3 weeks storage, as shown in Fig. S19.

4. Discussion

Up to now, changing the type or configuration of the probe molecules (Cai et al., 2014; Hajian et al., 2019; Hwang et al., 2018; Kong et al., 2021; Mei et al., 2018) or changing the sensing material (Hwang et al., 2020; Liang et al., 2020; Liu et al., 2019) of the FET sensor is still the

mainstream research direction to enhance FET's performance in detecting nucleic acid. In these studies, the probe molecules are immobilized on the surface of the sensing material to recognize and capture target nucleic acid molecules through complementary base pairing (Fu et al., 2017). The hybridization-driven mechanism for grabbing target molecules results in that one target molecule generate one unit signal and multiple target molecules linearly generates multiple unit signals. Here, we call the detection signal generated by capturing the target molecule in the hybridization mechanism as a "small addition" signal. Although the sensitivity of FET sensors has been improved a lot by these research works, the "small addition" signal generation mechanism prevents these sensors from showing a breakthrough sensitivity. Therefore, developing a new signal generation mechanism with higher efficiency is desirable. Here, thanks to the CRISPR-Cas13a system's strong cleavage properties to RP, the coupling of multiple CRISPRs, the optimized structure of RP and the highly sensitive electrical properties of GFETs, this collaborative system presented a "big subtraction" signal generating mechanism and obtained a higher intensity directional signal (more than 30%) compared with the detection signal (less than 7%) in similar graphene field-effect transistor (Wang et al., 2022a), and exhibits a lower detection limit of 0.15 copies/ μL, compared with the pure CRISPR/Cas13a technology (100 copies/ μL) (Fozouni et al., 2021), in detecting SARS-CoV-2 RNA.

For the GFET to detect the real samples of SARS-CoV-2, it must be considered that the RNA of SARS-CoV-2 is a single-stranded structure containing nearly 30,000 nucleic acid molecules, and the nucleosides of these 30,000 nucleic acids are very easy to form a non-cohesive valence binding with graphene. That leads to the fact that even without probe molecules, the RNA of SARS-CoV-2 can still be captured by graphene forcefully. The probe molecules of the traditional FET for detecting SARS-CoV-2 are usually composed of only dozens of nucleic acid molecules, but the corresponding dozens of target sites are hidden in a single-stranded structure containing 30,000 nucleic acid molecules. This makes it hard to believe that it is the probe molecules rather than graphene are responsible for capturing the target molecules to generate the detection signal. Therefore, it is necessary to develop a new signalling mechanism with higher specificity. Here, benefiting from the programmability of the CRISPR and the right-shifted characteristic detection signal ("Cut-E″ signal), untargeted RNAs adsorbed on the graphene produces the left-shifted characteristic enlarged E signal, but not the right-shifted characteristic "Cut-E signal". This mechanism makes the collaborative system achieve highly specificity to detecting SARS-CoV-2 RNA.

The volume of target RNAs extracted from clinical COVID-19 positive samples by commercial kits is usually from several microliters to several milliliters. At present, the size of the sensing material of the reported FET nucleic acid sensors is in the order of micrometers, and the scale of the liquid pool above the FET is designed to be in the order of millimeters (Dai et al., 2021; Kong et al., 2021; Seo et al., 2020; Wang et al., 2022a). By simple calculation, we can easily find that the area of the sensing material only accounts for a few thousandths of the liquid pool's surface, which means that the probability of a single SARS-CoV-2 RNA diffusing from the space of the liquid pool to the surface of the sensing material may be only one in a few million, or even lower. This means that even after a long diffusion time, only partial or even no target RNAs can diffuse to the surface of the sensing material and be caught by the probe molecules. Here, we believe that field-effect transistors based on micron-scale sensing materials have played an irreplaceable and positive role in scientific exploration at the laboratory level. However, the existing deficiencies make it necessary to develop the field-effect transistors based on larger-scale sensing materials to meet the needing for practical clinical testing. Here, benefiting from the large-area graphene with a centimeter diameter and a liquid storage tank of the same size (Fig. S7), the SARS-CoV-2 RNA & CRISPR-Cas13a analysis solution can fully and directly contact graphene & RP, which dramatically improves the probability of SARS-CoV-2 RNA & CRISPR-Cas13a diffusing from the liquid pool space to graphene & RP surface. This enables the collaborative system to achieve high-efficiency detection of SARS-CoV-2 RNA.

5. Conclusion

In the proposed collaborative system, SARS-CoV-2 RNAs can generate high-intensity signals with right shift features, and untargeted molecules generate left shift signals, eliminating the false-negative and false-positive signals effectively. The high sensitivity (0.25 aM) and high specificity caused by the opposite direction of the signals between targeted molecules and untargeted molecules, are not only of great significance for GFET to realize the effective detection of SARS-CoV-2 RNA but also very enlightening for GFET to realize the analysis and detection of other nucleic acid-related diseases. All the nucleic acid-related diseases are highly promising to be detected by our collaborative system by replacing the CRISPR-Cas system that specifically recognizes the related DNA/RNA targets. In addition, eliminating the instability of the field-effect transistor by hydrophobic treatment of it's substrate should greatly promote the engineering application of the field-effect transistor.

CRediT authorship contribution statement

Yang Sun: Conceptualization, Methodology, Software, Validation, Formal analysis, Investigation, Resources, Data curation, Visualization, Supervision, Project administration, Funding acquisition, Writing – original draft, Writing – review & editing. **Cheng Yang:** Conceptualization, Data curation, Writing – original draft, Writing – review & editing, Supervision. **Xiaolin Jiang:** Validation, Resources. **Pengbo Zhang:** Methodology, Software. **Shuo Chen:** Methodology, Software, Formal analysis. **Fengxia Su:** Resources. **Hui Wang:** Resources. **Weiliang Liu:** Validation, Writing – original draft. **Xiaofei He:** Investigation. **Lei Chen:** Supervision, Project administration. **Baoyuan Man:** Conceptualization, Project administration. **Zhengping Li:** Conceptualization, Methodology, Software, Validation, Formal analysis, Investigation, Resources, Data curation, Writing – original draft, Writing – review & editing, Visualization, Supervision, Project administration, Funding acquisition.

Declaration of competing interest

The authors declare that they have no known competing financial interests or personal relationships that could have appeared to influence the work reported in this paper.

Data availability

Data will be made available on request.

Acknowledgements

This study was funded by National Natural Science Foundation of China (21775012).

Appendix A. Supplementary data

Supplementary data to this article can be found online at https://doi.org/10.1016/j.bios.2022.114979.

References

Ang, P.K., Chen, W., Wee, A.T.S., Loh, K.P., 2008. Solution-gated epitaxial graphene as pH sensor. J. Am. Chem. Soc. 130 (44), 14392–14393.

Arons, M.M., Hatfield, K.M., Reddy, S.C., Kimball, A., James, A., Jacobs, J.R., Taylor, J., Spicer, K., Bardossy, A.C., Oakley, L.P., 2020. Presymptomatic SARS-CoV-2 infections and transmission in a skilled nursing facility. N. Engl. J. Med. 382 (22), 2081–2090.

Bokelmann, L., Nickel, O., Maricic, T., Pääbo, S., Meyer, M., Borte, S., Riesenberg, S., 2021. Point-of-care bulk testing for SARS-CoV-2 by combining hybridization capture with improved colorimetric LAMP. Nat. Commun. 12 (1), 1–8.
Bonanni, A., Chua, C.K., Zhao, G., Sofer, Z.k., Pumera, M., 2012. Inherently electroactive graphene oxide nanoplatelets as labels for single nucleotide polymorphism detection. ACS Nano 6 (10), 8546–8551.
Boyton, R.J., Altmann, D.M., 2021. The immunology of asymptomatic SARS-CoV-2 infection: what are the key questions? Nat. Rev. Immunol. 21 (12), 762–768.
Cai, B., Wang, S., Huang, L., Ning, Y., Zhang, Z., Zhang, G.-J., 2014. Ultrasensitive label-free detection of PNA–DNA hybridization by reduced graphene oxide field-effect transistor biosensor. ACS Nano 8 (3), 2632–2638.
Chan, J.F.-W., Kok, K.-H., Zhu, Z., Chu, H., To, K.K.-W., Yuan, S., Yuen, K.-Y., 2020. Genomic characterization of the 2019 novel human-pathogenic coronavirus isolated from a patient with atypical pneumonia after visiting Wuhan. Emerg. Microb. Infect. 9 (1), 221–236.
Chen, F., Qing, Q., Xia, J., Li, J., Tao, N., 2009. Electrochemical gate-controlled charge transport in graphene in ionic liquid and aqueous solution. J. Am. Chem. Soc. 131 (29), 9908–9909.
Chiu, U.-T., Lee, B.-F., Hu, S.-K., Yu, T.-F., Lee, W.-Y., Chao, L., 2019. Graphene memory based on a tunable nanometer-thin water layer. J. Phys. Chem. C 123 (17), 10842–10848.
Cohen, A.N., Kessel, B., Milgroom, M.G., 2020. Diagnosing SARS-CoV-2 infection: the danger of over-reliance on positive test results. medRxiv. https://doi.org/10.1101/2020.04.26.20080911.
Cortés-Arriagada, D., 2021. Intermolecular driving forces on the adsorption of DNA/RNA nucleobases to graphene and phosphorene: an atomistic perspective from DFT calculations. J. Mol. Liq. 325, 115229.
Dai, C., Guo, M., Wu, Y., Cao, B.-P., Wang, X., Wu, Y., Kang, H., Kong, D., Zhu, Z., Ying, T., 2021. Ultraprecise antigen 10-in-1 pool testing by multiantibodies transistor assay. J. Am. Chem. Soc. 143 (47), 19794–19801.
Das, A., Pisana, S., Chakraborty, B., Piscanec, S., Saha, S.K., Waghmare, U.V., Novoselov, K.S., Krishnamurthy, H.R., Geim, A.K., Ferrari, A.C., 2008. Monitoring dopants by Raman scattering in an electrochemically top-gated graphene transistor. Nat. Nanotechnol. 3 (4), 210–215.
Dollekamp, E., Bampoulis, P., Faasen, D.I.P., Zandvliet, H.J., Kooij, E.S., 2017. Charge induced dynamics of water in a graphene–mica slit pore. Langmuir 33 (43), 11977–11985.
Eisenstein, M., 2022. Seven technologies to watch in 2022. Nature 601 (7894), 658–661.
Elder, R.M., Jayaraman, A., 2013. Structure and thermodynamics of ssDNA oligomers near hydrophobic and hydrophilic surfaces. Soft Matter 9 (48), 11521–11533.
Fozouni, P., Son, S., de León Derby, M.D., Knott, G.J., Gray, C.N., D'Ambrosio, M.V., Zhao, C., Switz, N.A., Kumar, G.R., Stephens, S.I., 2021. Amplification-free detection of SARS-CoV-2 with CRISPR-Cas13a and mobile phone microscopy. Cell 184 (2), 323–333 e329.
Fu, W., Jiang, L., van Geest, E.P., Lima, L.M., Schneider, G.F., 2017. Sensing at the surface of graphene field-effect transistors. Adv. Mater. 29 (6), 1603610.
Gao, Z., Xia, H., Zauberman, J., Tomaiuolo, M., Ping, J., Zhang, Q., Ducos, P., Ye, H., Wang, S., Yang, X., 2018. Detection of sub-fM DNA with target recycling and self-assembly amplification on graphene field-effect biosensors. Nano Lett. 18 (6), 3509–3515.
Gao, J., Wang, C., Chu, Y., Han, Y., Gao, Y., Wang, Y., Wang, C., Liu, H., Han, L., Zhang, Y., 2022. Graphene oxide-graphene Van der Waals heterostructure transistor biosensor for SARS-CoV-2 protein detection. Talanta 240, 123197.
Gootenberg, J.S., Abudayyeh, O.O., Lee, J.W., Essletzbichler, P., Dy, A.J., Joung, J., Verdine, V., Donghia, N., Daringer, N.M., Freije, C.A., 2017. Nucleic acid detection with CRISPR-Cas13a/C2c2. Science 356 (6336), 438–442.
Hajian, R., Balderston, S., Tran, T., DeBoer, T., Etienne, J., Sandhu, M., Wauford, N.A., Chung, J.-Y., Nokes, J., Athaiya, M., 2019. Detection of unamplified target genes via CRISPR–Cas9 immobilized on a graphene field-effect transistor. Nat. Biomed. Eng 3 (6), 427–437.
Hinnemo, M., Zhao, J., Ahlberg, P., Hagglund, C., Djurberg, V., Scheicher, R.H., Zhang, S.-L., Zhang, Z.-B., 2017. On monolayer formation of pyrenebutyric acid on graphene. Langmuir 33 (15), 3588–3593.
Hong, Y., Wang, S., Li, Q., Song, X., Wang, Z., Zhang, X., Besenbacher, F., Dong, M., 2019. Interfacial icelike water local doping of graphene. Nanoscale 11 (41), 19334–19340.
Hu, S.-K., Lo, F.-Y., Hsieh, C.-C., Chao, L., 2019. Sensing ability and formation criterion of fluid supported lipid bilayer coated graphene field-effect transistors. ACS Sens. 4 (4), 892–899.
Hwang, M.T., Wang, Z., Ping, J., Ban, D.K., Shiah, Z.C., Antonschmidt, L., Lee, J., Liu, Y., Karkisaval, A.G., Johnson, A.T.C., 2018. DNA nanotweezers and graphene transistor enable label-free genotyping. Adv. Mater. 30 (34), 1802440.
Hwang, M.T., Heiranian, M., Kim, Y., You, S., Leem, J., Taqieddin, A., Faramarzi, V., Jing, Y., Park, I., van der Zande, A.M., 2020. Ultrasensitive detection of nucleic acids using deformed graphene channel field effect biosensors. Nat. Commun. 11 (1), 1–11.
Kaminski, M.M., Abudayyeh, O.O., Gootenberg, J.S., Zhang, F., Collins, J.J., 2021. CRISPR-based diagnostics. Nat. Biomed. Eng 5 (7), 643–656.
Kevadiya, B.D., Machhi, J., Herskovitz, J., Oleynikov, M.D., Blomberg, W.R., Bajwa, N., Soni, D., Das, S., Hasan, M., Patel, M., 2021. Diagnostics for SARS-CoV-2 infections. Nat. Mater. 20 (5), 593–605.
Kong, D., Wang, X., Gu, C., Guo, M., Wang, Y., Ai, Z., Zhang, S., Chen, Y., Liu, W., Wu, Y., 2021. Direct SARS-CoV-2 nucleic acid detection by Y-shaped DNA dual-probe transistor assay. J. Am. Chem. Soc. 143 (41), 17004–17014.
Lee, M.J., Choi, J.S., Kim, J.-S., Byun, I.-S., Lee, D.H., Ryu, S., Lee, C., Park, B.H., 2012. Characteristics and effects of diffused water between graphene and a SiO2 substrate. Nano Res. 5 (10), 710–717.
Lee, D., Ahn, G., Ryu, S., 2014. Two-dimensional water diffusion at a graphene–silica interface. J. Am. Chem. Soc. 136 (18), 6634–6642.
Liang, Y., Xiao, M., Wu, D., Lin, Y., Liu, L., He, J., Zhang, G., Peng, L.-M., Zhang, Z., 2020. Wafer-scale uniform carbon nanotube transistors for ultrasensitive and label-free detection of disease biomarkers. ACS Nano 14 (7), 8866–8874.
Liu, J., Chen, X., Wang, Q., Xiao, M., Zhong, D., Sun, W., Zhang, G., Zhang, Z., 2019. Ultrasensitive monolayer MoS_2 field-effect transistor based DNA sensors for screening of down syndrome. Nano Lett. 19 (3), 1437–1444.
Liu, R., Han, H., Liu, F., Lv, Z., Wu, K., Liu, Y., Feng, Y., Zhu, C., 2020. Positive rate of RT-PCR detection of SARS-CoV-2 infection in 4880 cases from one hospital in Wuhan, China, from Jan to Feb 2020. Clin. Chim. Acta 505, 172–175.
Long, Q.-X., Tang, X.-J., Shi, Q.-L., Li, Q., Deng, H.-J., Yuan, J., Hu, J.-L., Xu, W., Zhang, Y., Lv, F.-J., 2020. Clinical and immunological assessment of asymptomatic SARS-CoV-2 infections. Nat. Med. 26 (8), 1200–1204.
Manna, A.K., Pati, S.K., 2013. Theoretical understanding of single-stranded DNA assisted dispersion of graphene. J. Mater. Chem. B 91–100.
Mao, S., Chang, J., Pu, H., Lu, G., He, Q., Zhang, H., Chen, J., 2017. Two-dimensional nanomaterial-based field-effect transistors for chemical and biological sensing. Chem. Soc. Rev. 46 (22), 6872–6904.
Mei, J., Li, Y.-T., Zhang, H., Xiao, M.-M., Ning, Y., Zhang, Z.-Y., Zhang, G.-J., 2018. Molybdenum disulfide field-effect transistor biosensor for ultrasensitive detection of DNA by employing morpholino as probe. Biosens. Bioelectron. 110, 71–77.
Nath, H., Mallick, A., Roy, S., Sukla, S., Basu, K., De, A., Biswas, S., 2021. Archived dengue serum samples produced false-positive results in SARS-CoV-2 lateral flow-based rapid antibody tests. J. Med. Microbiol. 70 (6), 001369.
Novoselov, K.S., Geim, A.K., Morozov, S.V., Jiang, D.-e., Zhang, Y., Dubonos, S.V., Grigorieva, I.V., Firsov, A.A., 2004. Electric field effect in atomically thin carbon films. Science 306 (5696), 666–669.
Orooji, Y., Sohrabi, H., Hemmat, N., Oroojalian, F., Baradaran, B., Mokhtarzadeh, A., Mohaghegh, M., Karimi-Maleh, H., 2021. An overview on SARS-CoV-2 (COVID-19) and other human coronaviruses and their detection capability via amplification assay, chemical sensing, biosensing, immunosensing, and clinical assays. Nano-Micro Lett. 13 (1), 1–30.
Ranganathan, S.V., Halvorsen, K., Myers, C.A., Robertson, N.M., Yigit, M.V., Chen, A.A., 2016. Complex thermodynamic behavior of single-stranded nucleic acid adsorption to graphene surfaces. Langmuir 32 (24), 6028–6034.
Schedin, F., Geim, A.K., Morozov, S.V., Hill, E., Blake, P., Katsnelson, M., Novoselov, K. S., 2007. Detection of individual gas molecules adsorbed on graphene. Nat. Mater. 6 (9), 652–655.
Seo, G., Lee, G., Kim, M.J., Baek, S.-H., Choi, M., Ku, K.B., Lee, C.-S., Jun, S., Park, D., Kim, H.G., 2020. Rapid detection of COVID-19 causative virus (SARS-CoV-2) in human nasopharyngeal swab specimens using field-effect transistor-based biosensor. ACS Nano 14 (4), 5135–5142.
Sitjar, J., Liao, J.-D., Lee, H., Tsai, H.-P., Wang, J.-R., Liu, P.-Y., 2021. Challenges of SERS technology as a non-nucleic acid or-antigen detection method for SARS-CoV-2 virus and its variants. Biosens. Bioelectron. 181, 113153.
Smyrlaki, I., Ekman, M., Lentini, A., Rufino de Sousa, N., Papanicolaou, N., Vondracek, M., Aarum, J., Safari, H., Muradrasoli, S., Rothfuchs, A.G., 2020. Massive and rapid COVID-19 testing is feasible by extraction-free SARS-CoV-2 RT-PCR. Nat. Commun. 11 (1), 1–12.
Song, L., Xiao, G., Zhang, X., Gao, Z., Sun, S., Zhang, L., Feng, Y., Luan, G., Lin, S., He, M., 2020. A case of SARS-CoV-2 carrier for 32 days with several times false negative nucleic acid tests. medRxiv. https://doi.org/10.1101/2020.03.31.20045401.
Stern, E., Wagner, R., Sigworth, F.J., Breaker, R., Fahmy, T.M., Reed, M.A., 2007. Importance of the Debye screening length on nanowire field effect transistor sensors. Nano Lett. 7 (11), 3405–3409.
Surkova, E., Nikolayevskyy, V., Drobniewski, F., 2020. False-positive COVID-19 results: hidden problems and costs. Lancet Respir. Med. 8 (12), 1167–1168.
Swank, Z., Michielin, G., Yip, H.M., Cohen, P., Andrey, D.O., Vuilleumier, N., Kaiser, L., Eckerle, I., Meyer, B., Maerkl, S.J., 2021. A high-throughput microfluidic nanoimmunoassay for detecting anti–SARS-CoV-2 antibodies in serum or ultralow-volume blood samples. P Natl. A. Sci 118 (18), e2025289118.
Talebian, S., Wallace, G.G., Schroeder, A., Stellacci, F., Conde, J., 2020. Nanotechnology-based disinfectants and sensors for SARS-CoV-2. Nat. Nanotechnol. 15 (8), 618–621.
Tan, Y.-W., Zhang, Y., Bolotin, K., Zhao, Y., Adam, S., Hwang, E., Sarma, S.D., Stormer, H., Kim, P., 2007. Measurement of scattering rate and minimum conductivity in graphene. Phys. Rev. Lett. 99 (24), 246803.
Tang, Y., Gao, L., Feng, W., Guo, C., Yang, Q., Li, F., Le, X.C., 2021. The CRISPR–Cas toolbox for analytical and diagnostic assay development. Chem. Soc. Rev. 50, 11844–11869.
Wang, Z., Yi, K., Lin, Q., Yang, L., Chen, X., Chen, H., Liu, Y., Wei, D., 2019. Free radical sensors based on inner-cutting graphene field-effect transistors. Nat. Commun. 10 (1), 1–10.
Wang, Z., Hao, Z., Wang, X., Huang, C., Lin, Q., Zhao, X., Pan, Y., 2021. A flexible and regenerative aptameric graphene–Nafion biosensor for cytokine storm biomarker monitoring in undiluted biofluids toward wearable applications. Adv. Funct. Mater. 31 (4), 2005958.
Wang, L., Wang, X., Wu, Y., Guo, M., Gu, C., Dai, C., Kong, D., Wang, Y., Zhang, C., Qu, D., 2022a. Rapid and ultrasensitive electromechanical detection of ions, biomolecules and SARS-CoV-2 RNA in unamplified samples. Nat. Biomed. Eng 6 (3), 276–285.

Wang, Z., Hao, Z., Yang, C., Wang, H., Huang, C., Zhao, X., Pan, Y., 2022b. Ultra-sensitive and rapid screening of acute myocardial infarction using 3D-affinity graphene biosensor. Cell Rep. Phys. Sci 5 (3), 100855.
Welch, N.L., Zhu, M., Hua, C., Weller, J., Mirhashemi, M.E., Nguyen, T.G., Mantena, S., Bauer, M.R., Shaw, B.M., Ackerman, C.M., 2022. Multiplexed CRISPR-based microfluidic platform for clinical testing of respiratory viruses and identification of SARS-CoV-2 variants. Nat. Med. 1-1.
Woloshin, S., Patel, N., Kesselheim, A.S., 2020. False negative tests for SARS-CoV-2 infection—challenges and implications. N. Engl. J. Med. 383 (6), e38.
Wu, G., Tang, X., Meyyappan, M., Lai, K.W.C., 2017. Doping effects of surface functionalization on graphene with aromatic molecule and organic solvents. Appl. Surf. Sci. 425, 713–721.
Yang, Y., Peng, Y., Lin, C., Long, L., Hu, J., He, J., Zeng, H., Huang, Z., Li, Z.-Y., Tanemura, M., 2021. Human ACE2-functionalized gold "virus-trap" nanostructures for accurate capture of SARS-CoV-2 and single-virus SERS detection. Nano-Micro Lett. 13 (1), 1–13.
Zhang, Y., Yuan, S., Zhou, W., Xu, J., Li, Y., 2007. Spectroscopic evidence and molecular simulation investigation of the π–π interaction between pyrene molecules and carbon nanotubes. J. Nanosci. Nanotechnol. 7 (7), 2366–2375.